International Journal of Engineering and Technology Innovation, vol. 14, no. 4, 2024, pp. 407-422

Billet Size Optimization for Hot Forging of AISI 1045 Medium Carbon Steel Using Zener-Hollomon and Cingara-McQueen Model

Naiyanut Jantepa, Nattarawee Siripath, Surasak Suranuntchai*

Department of Tool and Materials Engineering, Faculty of Engineering, King Mongkut's University of Technology Thonburi, Bangkok, Thailand

Received 24 January 2024; received in revised form 10 May 2024; accepted 11 May 2024

DOI: https://doi.org/10.46604/ijeti.2024.13302

Abstract

This study investigates the effects of initial billet size variations on material flow behavior in hot forging processes, aiming to optimize the forging process using validated predictive models. Material and high-temperature compressive tests inform mathematical models, while simulations are conducted via the finite element method (FEM). Results align with the Zener-Hollomon and Cingara-McQueen approaches. The Arrhenius model predicts AISI 1045 steel flow stress with an R^2 of 0.968 and an average absolute relative error (AARE) of 7.079%. The Cingara-McQueen equation achieves an R^2 of 0.997 and an AARE of 2.960%. Reducing billets size from 260 mm to 230 mm decreases the material usage by up to 11.5%, while maintaining workpiece integrity. Experimental and simulated loads exhibit an AARE of about 2.69%, thereby indicating potential cost and efficiency improvements in hot forging processes.

Keywords: hot forging, compressive tests, Zener-Hollomon, Cingara-McQueen, AISI 1045 carbon steel

1. Introduction

Hot forging involves the shaping of metal at high temperatures and is a widely used manufacturing technique in various industries, including automotive, aerospace, and construction. The metal is typically heated to a temperature beyond its recrystallization temperature, where it becomes more malleable and accessible to deformation. The forging process then transforms the heated metal into the desired shape by the application of compressive force, often via a press or hammer [1].

Despite its longstanding significance, the forging industry faces challenges from alternative manufacturing methods. However, the advent of advanced computational techniques, particularly finite element method (FEM) simulations, offers promising avenues for addressing these challenges [2]. Hot forging processes have evolved significantly in the realm of advanced materials engineering and computational modeling. Engineers and researchers are continually seeking ways to enhance the precision and reliability of hot forging [3].

The efficiency and quality of hot forging depend on several critical factors, including material properties, temperature control, die design, forging load, post-forging processes, lubrication, equipment conditions, environmental factors, and quality control, all of which play essential roles. In this context, the initial billet size is an important factor affecting the material utilization, mechanical properties, microstructure, and overall performance of the forged product. Therefore, optimization of the billet size is crucial for achieving cost-effective and high-quality forged components. Traditionally, the selection of billet size has relied on empirical methods and experiential knowledge. However, with advanced modeling techniques and metallurgical theories, it is now possible to employ a more scientific approach to determine the ideal billet size.

* Corresponding author. E-mail address: surasak.sur@kmutt.ac.th

English language proofreader: Yen-Chun Hsieh

Since 2022, the recent literature has highlighted advancements in hot forging processes. For instance, Soranansri, et al. [3] emphasized the critical role of process design and billet size in the hot forging industry, underscoring their impact on product quality and material efficiency. Their study introduced a novel approach using FEM to design the hot forging process, particularly for talar body prostheses. The FEM optimization of the initial billet size enabled significant improvements in material utilization and process efficiency, demonstrating a remarkable 2.6-fold increase compared to conventional methods. Similarly, a recent study utilized three-dimensional (3D) FEM with the QForm software to optimize the initial billet size for the hot forging of commercial SNCM8 steel alloy upper ball joints. Notably, the practical reduction of billet length while maintaining a constant diameter yielded a defect-free final product, thereby underscoring the importance of precise parametric optimization [4].

In addition, an understanding of the material flow behavior during hot working plays a pivotal role in developing the optimal hot working conditions, and various processing parameters significantly influence this understanding [5]. A constitutive model is a framework used to describe how metallic systems respond to multiple factors during hot deformation processes such as forging and rolling. It considers parameters such as temperature, strain, and deformation rates to analyze the metal behavior. Given the challenge of predicting flow behavior at high temperatures, accurate constitutive models are essential for numerical simulations and analytical studies of metal forming. Researchers have dedicated significant efforts to refining these models, leading to advancements in the understanding and optimization of metalworking techniques [6-7].

For instance, the Zener-Hollomon parameter, which is rooted in deformation kinetics, is a valuable tool for predicting a material's flow behavior during hot deformation processes. It considers the strain rate, temperature, and material properties to characterize the deformation accurately. As a component of the Arrhenius model, it forecasts the flow stress based on the strain, temperature, and strain rate, with the hyperbolic sine, exponential, and power functions enhancing its predictive capacity, especially for materials under varying stress levels.

Previous attempts have been made to apply constitutive equations to alloys such asTi-45Al-8Nb-2Cr-2Mn-0.2Y alloy [8], BS 080M46 medium carbon steel [9], Fe–23Mn–2Al–0.2C twinning induced plasticity (TWIP) steel [10], 1.4542 stainless steel [11], SNCM8 alloy steel [12], etc. Additionally, the Cingara-McQueen variables, which are primarily described in the pre-peak range of a given curve, provide a means to quantify the effects of strain, strain rate, and temperature on the material behavior during plastic deformation. These variables offer a comprehensive framework for analyzing and optimizing hot forging processes [12-15].

Despite significant advancements in modeling the hot forging process, critical gaps remain, particularly concerning the selection of initial billet size and the understanding of material flow behavior during hot working. Hence, the present study aims to fill the remaining knowledge gaps to optimize the hot forging process. To this end, the study utilizes the QForm V10.1.6 software to simulate the hot forging process of an AISI 1045 carbon steel auto part to optimize the initial billet size by examining the effects of various sizes on the response of the forged parts while analyzing the process under various forming loads. Further, the high-temperature flow behavior is predicted by using the Arrhenius model with either the Zener-Hollomon parameter or the Cingara-McQueen variables obtained via hot compressive tests. This comprehensive approach is aimed at advancing the understanding and efficiency of the hot forging processes to address the challenges faced by the forging industry and to enhance the competitiveness of hot forging as a manufacturing technique.

2. Experimental Procedure and Material Testing

The study employs material composition analysis and hot-compressive testing as the basis for evaluating the properties and performance of the materials under investigation. Through characterization of the material's composition and exposure to

controlled compressive forces at elevated temperatures, crucial insights into its response to stress and strain are attained. This comprehensive methodology facilitates the prediction of the material's behavior in practical applications and the identification of potential limitations or optimization opportunities.

2.1. Chemical composition of the AISI 1045 carbon steel

The material used in this research is AISI 1045 steel. It is classified as a medium carbon low alloy steel and is essential in various industries, particularly automotive and machinery. This type of steel is widely employed in producing various components, especially in applications that demand high strength, including screws, gears, drive shafts, threaded rods, piston rods, and more. The standard chemical composition of AISI 1045 carbon steel is presented in Table 1 [16].

Table 1 The standard chemical composition of AISI 1045 carbon steel (wt.%)

C	Mn	Si	P	S	Ni	Cr	Mo
0.36-0.43	0.60-0.90	0.15-0.35	0.03Max.	0.03Max.	1.60-2.00	0.60-1.00	0.15-0.30

In the present study, the chemical compositions of two test specimens were determined using an emission spectrometer for validation. The specimens (S.B.-CERA Co., Ltd.) were chemically checked at three points each following the ASTM E59-93 guidelines and the Iron and Steel Institute of Thailand procedure to ensure that their chemical compositions were comparable with AISI standards. The results are summarized in Table 2, indicating that the alloy steel contains elements such as carbon (C), nickel (Ni), chromium (Cr), and molybdenum (Mo) in comparable amounts to the standard composition shown in Table 1. These elements contribute to its high strength, hardenability, and corrosion resistance.

Table 2 The measured chemical compositions of the AISI 1045 carbon steel samples (wt.%)

Sample	C	Si	Mn	P	S	Ni	Cr	Mo	Cu	Mg	Al	Ti
(1)	0.387	0.274	0.694	0.025	0.016	1.864	0.768	0.155	0.095	0.001	0.024	0.001
(2)	0.387	0.273	0.695	0.026	0.017	1.879	0.767	0.156	0.094	0.001	0.016	0.001
Avg.	0.387	0.273	0.695	0.025	0.017	1.871	0.768	0.156	0.094	0.001	0.02	0.001

2.2. High-temperature compressive test

In this study, a deformation dilatometer (TA Instruments, DIL805) was used to enable controlled heating and cooling of the samples within either a controlled or ambient environment (Fig. 1). This apparatus can deform and reshape the samples, as well as allow control over the cooling rate after deformation. This is advantageous for replicating conditions that closely mimic the manufacturing process on a small scale. Moreover, it facilitates the analysis of various properties of the experimental samples, including the phase composition, grain size, morphology, elemental precipitates, and hardness.

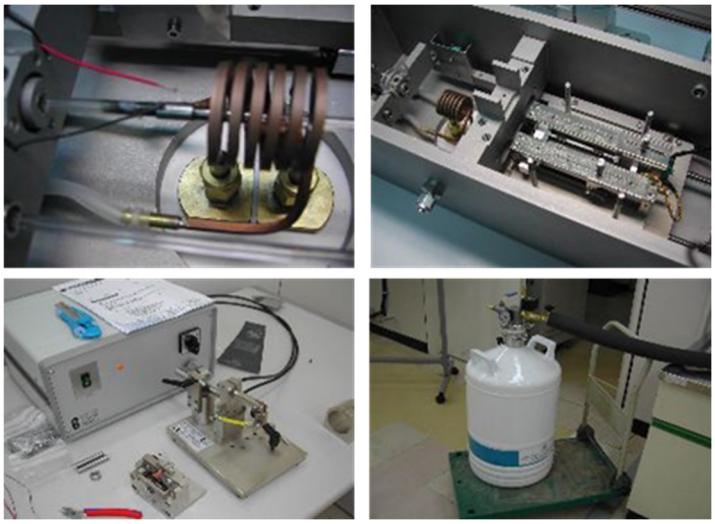

Fig. 1 The deformation dilatometer equipment

The versatility of the deformation dilatometer renders it an indispensable tool in metallurgical research and development. It enables precise exploration of the material behavior under specific conditions, which is a crucial aspect of optimizing manufacturing processes and ensuring product quality [17]. In the present work, cylindrical AISI 1045 test specimens measuring 5 mm in diameter and 10 mm in length were used. The study was conducted at temperatures of 900, 1000, 1100, and 1200 ℃, with constant strain rates of 0.1, 1, and 10 s^{-1}. These examinations were performed at the Iron and Steel Institute of Thailand.

The experimental protocol for the hot compressive test is shown schematically in Fig. 2. To minimize friction between the specimen's surface and the ceramic die, 0.1 mm-thick molybdenum sheets were applied on both sides of the test specimen. Following previous studies, the initial heating rate was approximately 10 ℃/s [18], and the sample was held at the target temperature for 60 seconds to ensure uniform heating throughout. After that, the specimen was subjected to hot deformation at a constant strain rate, with the application of 60% strain in its height. Finally, rapid cooling was achieved using nitrogen gas, with a cooling rate of 40 ℃/s [19]. The outcomes were graphically represented in the form of flow stress-strain curves. This dataset was further analyzed to derive a constitutive equation that characterizes the material's plastic behavior during hot deformation, encompassing both viscoelasticity and strain-hardening aspects within a plasticity model.

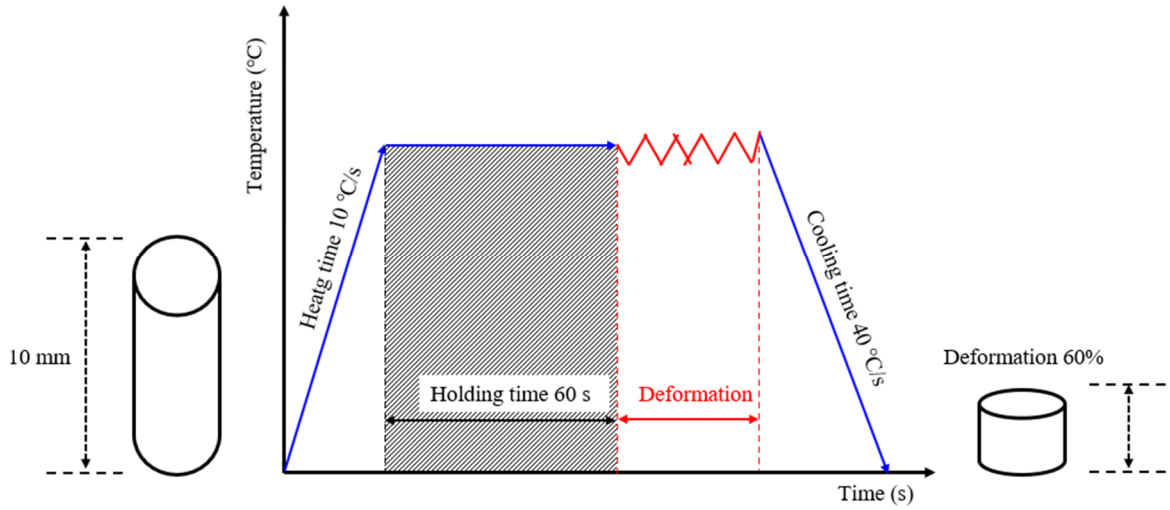

Fig. 2 A schematic diagram of the hot compressive test

3. Developing the Constitutive Model

In this section, the development of a constitutive model that is capable of mathematically capturing the observed behavior of the material during hot compressive testing is discussed. This model comprises an equation or set of equations that describe the relationship between stress and strain for the material. By integrating the experimental data into the model, accurate predictions of the material's response under various loading conditions and temperatures can be made. This predictive capability will prove instrumental for subsequent analysis and design optimization.

3.1. The flow stress-strain curves

The relationship between the material's true stress and true strain is elucidated by the results of the hot compressive tests conducted at strain rates of 0.1, 1, and 10 s^{-1} and temperatures of 900, 1000, 1100, and 1200 ℃ in Fig. 3. Here, a typical flow behavior is consistently observed across all three strain rates, wherein the flow stress decreases as the temperature increases and as the strain rate decreases. At a strain rate of 0.1 s^{-1} and a temperature of 900 ℃ (Fig. 3(a)) the true stress increases gradually to a maximum value of about 150 MPa at a true strain of around 1.17 and then decreases gradually with the further increase in true strain. Similar behaviors are observed at other temperatures and strain rates. This phenomenon arises from the interplay between strain hardening and strain softening mechanisms.

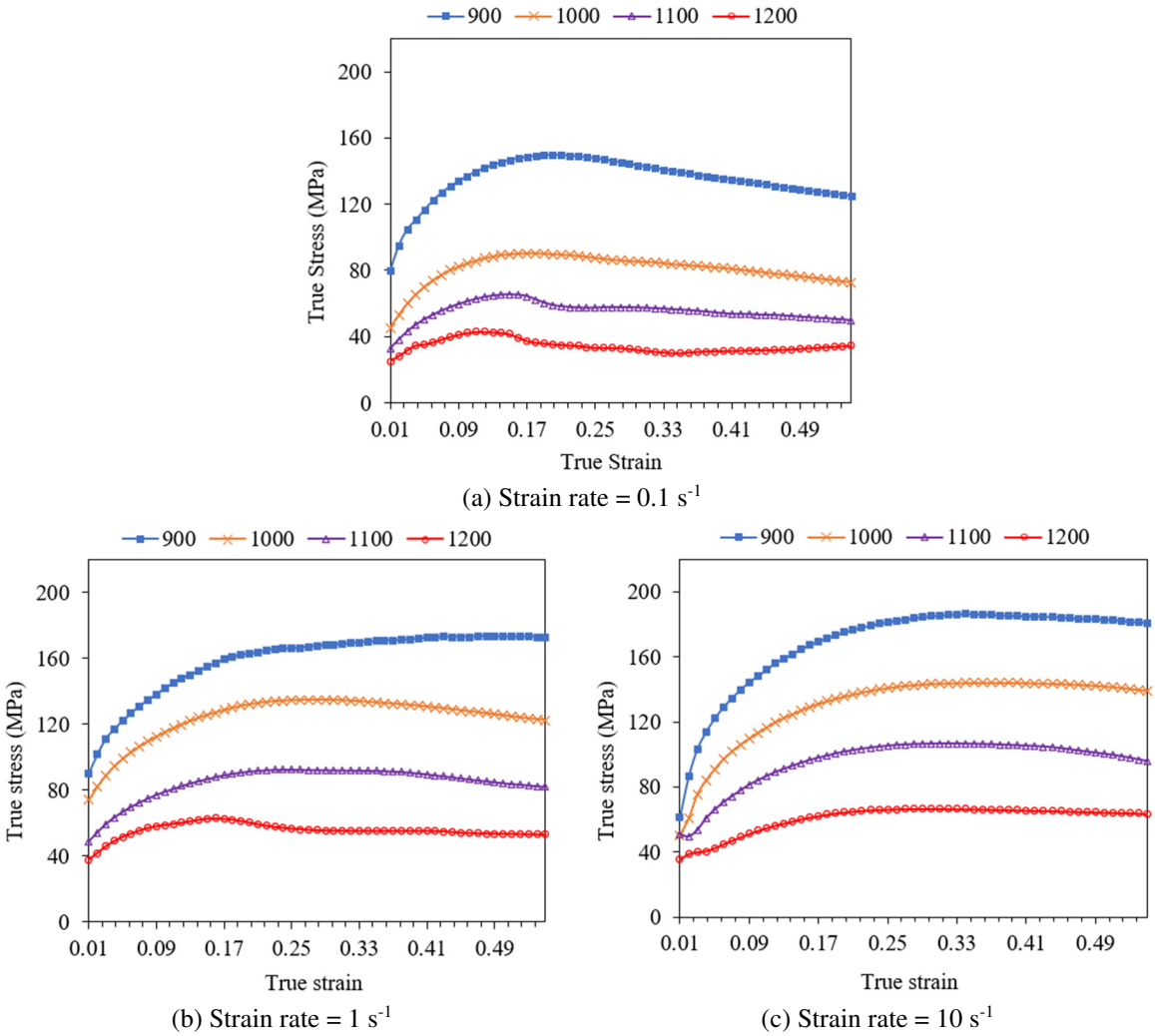

(a) Strain rate = 0.1 s^{-1}

(b) Strain rate = 1 s^{-1}

(c) Strain rate = 10 s^{-1}

Fig. 3 True stress-strain curves from the Hot compressive test

When the material's hardening rate exceeds its softening rate, there is adequate energy for strain-hardening to occur at maximum stress. The flow stress then consistently decreases until a balance is achieved between the strain softening and strain hardening mechanisms, thus resulting in a steady-state condition. This observation highlights the significance of flow behavior in hot compressive testing, which provides valuable insights into the deformation characteristics of materials at elevated temperatures and strain rates. Such insights enable manufacturers and designers to make informed decisions, optimize processes, and design components that are tailored for high-temperature applications. This, in turn, drives advancements in industrial practices and product performance.

3.2. Predicting the material's flow behavior via the Arrhenius model with the Zener-Hollomon parameter

In this section, the results obtained from hot compressive tests on AISI 1045 steel will reveal strain hardening and strain softening mechanisms within the true stress and true strain relationship. Consequently, a constitutive equation is developed based on the Arrhenius model, which describes the relationship between flow stress, strain rate, and temperature. Here, the influence of temperature and strain rate on the flow behavior is depicted using the Zener-Hollomon parameter, as defined in:

$$Z = \dot{\varepsilon} \exp\left(Q/RT\right) \tag{1}$$

The relevant material constants required for the Arrhenius model can be directly determined from experimental data. This model typically consists of three functions [9, 20-21].

$$\dot{\varepsilon} = AF\left(\sigma\right)\exp\left(-Q/RT\right) \tag{2}$$

The first function is the power-law function, which may not accurately represent high-stress conditions ($\alpha\sigma > 0.8$).

$$\dot{\varepsilon} = A\sigma^{n_1} \exp(-Q/RT) \tag{3}$$

The second function is the exponential law, which may not accurately describe material behavior at low stress levels ($\alpha\sigma < 1.2$).

$$\dot{\varepsilon} = A \exp(\beta\sigma) \exp(-Q/RT) \tag{4}$$

The third function is the hyperbolic-sine law. This function is used to model the entire range of strains.

$$\dot{\varepsilon} = A(\sinh \alpha\sigma)^{n_2} \exp(-Q/RT) \tag{5}$$

Hence, the present study incorporates the hyperbolic-sine function into the Arrhenius model to comprehensively describe the material's flow behavior, as outlined below. Where $\dot{\varepsilon}$ is strain rate (s^{-1}), while A, α, β, n_1, and n_2 are the material parameters. which is $\alpha = \beta/n_1$, α is flow stress (MPa) used to determine stress, R is the standard gas constant (8.314 $Jmol^{-1}K^{-1}$), Q represents the activation energy during hot deformation ($kJmol^{-1}$), and T is the temperature (K). The variables n_1 and β are derived from Eqs. (3) and (4) by applying the natural logarithm to both sides of each equation.

Subsequently, it will be used in the formula as follows:

$$\ln \dot{\varepsilon} = n_1 \ln \sigma + \ln A - (Q/RT) \tag{6}$$

$$\ln \dot{\varepsilon} = \beta\sigma + \ln A - (Q/RT) \tag{7}$$

The differences between Eqs. (6) and (7) at elevated temperatures during the hot compressive process are considered by taking into account the variations in flow stress as follows:

$$\left[\frac{\partial \ln \dot{\varepsilon}}{\partial \ln \sigma}\right]_T = n_1 \tag{8}$$

$$\left[\frac{\partial \ln \dot{\varepsilon}}{\partial \sigma}\right]_T = \beta \tag{9}$$

Therefore, the material constants n_1 and β will be determined by using the linear regression method to establish the relationship between $\ln\dot{\varepsilon}$ and $\ln\sigma$ as well as that between $\ln\dot{\varepsilon}$ and σ at various deformation temperatures, as depicted in Figs. 4(a) and 4(b). The values of n_1 and β derived from the hot compressive test result at a given temperature and strain rate represent critical parameters. The average values of n_1 and β for all specified temperatures are calculated to be 11.6061 and 0.1184, respectively, with an α value of 0.0102.

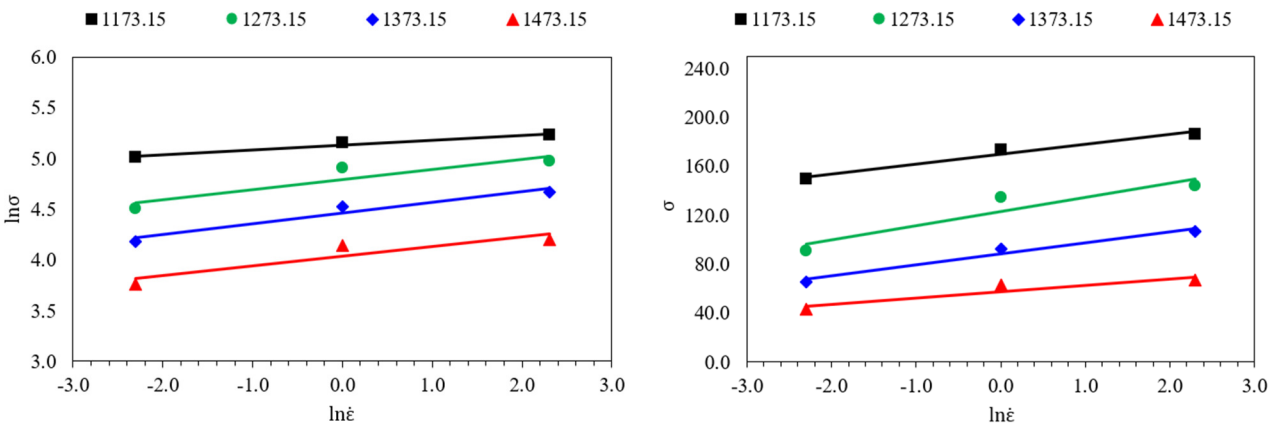

(a) n_1 (b) β

Fig. 4 The linear regressions for determining the parameters of n_1 and β

A similar calculation process, resembling the method employed for determining the material parameter n_1, will be utilized to derive the variable n_2 from Eq. (5). This will involve taking the natural logarithms on both sides of the equation, resulting in the following:

$$\ln \dot{\varepsilon} = n_2 \ln\left[\sinh\left(\alpha\sigma\right)\right] + \ln A - \left(Q/RT\right) \tag{10}$$

$$\left[\frac{\partial \ln \dot{\varepsilon}}{\partial \ln\left\{\sinh\left(\alpha\sigma\right)\right\}}\right]_T = n_2 \tag{11}$$

The value of n_2 is determined at each deformation temperature by applying the linear regression method to the relationship between $\ln\dot{\varepsilon}$ and $\ln[\sinh(\alpha\sigma)]$, as shown in Fig. 5(a). The average value of n_2 for all experimental temperatures is calculated to be 8.1297. The value of Q for elevated temperatures can be obtained from Eq. (10) as follows:

$$\ln\left[\sinh\left(\alpha\sigma\right)\right] = \left(Q/n_2RT\right) + \left(\ln \dot{\varepsilon}/n_2\right) - \left(\ln A/n_2\right) \tag{12}$$

$$\left[\frac{\partial \ln\left\{\sinh\left(\alpha\sigma\right)\right\}}{\partial\left(1/T\right)}\right] = \frac{Q}{n_2 R} \tag{13}$$

$$Q = Rn_2\left[\frac{\partial \ln\left\{\sinh\left(\alpha\sigma\right)\right\}}{\partial\left(1/T\right)}\right] \tag{14}$$

Thus, the Q value is determined by using the linear regression method for the relationship between $\ln[\sinh(\alpha\sigma)]$ and $1000/T$, based on the result of the strain rate study, as shown in Fig. 5(b). This allows the Q value to be calculated for each strain rate and temperature. The average Q value for the AISI 1045 material is calculated to be 577.21 kJ/mol.

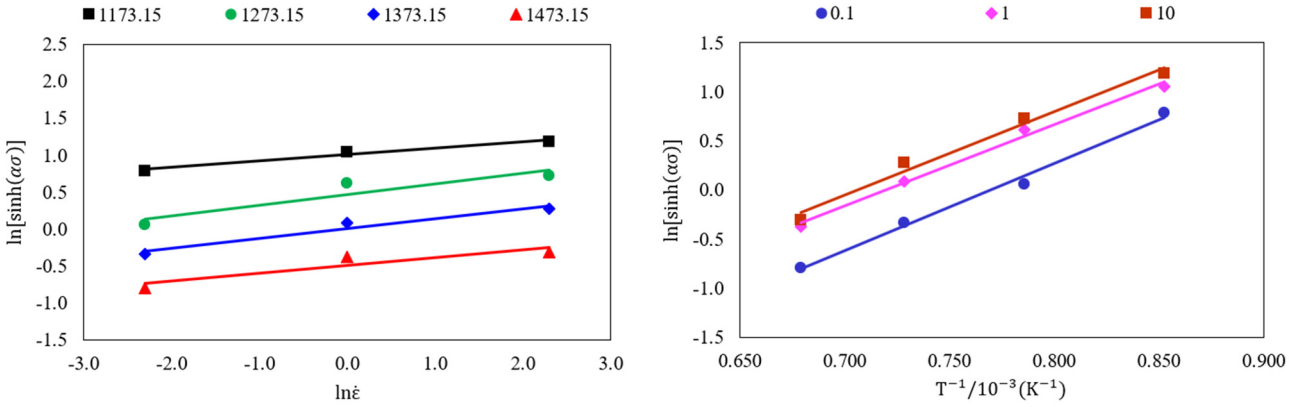

(a) n_2 (b) Q

Fig. 5 The linear regressions for determining the parameters of n_2 and Q

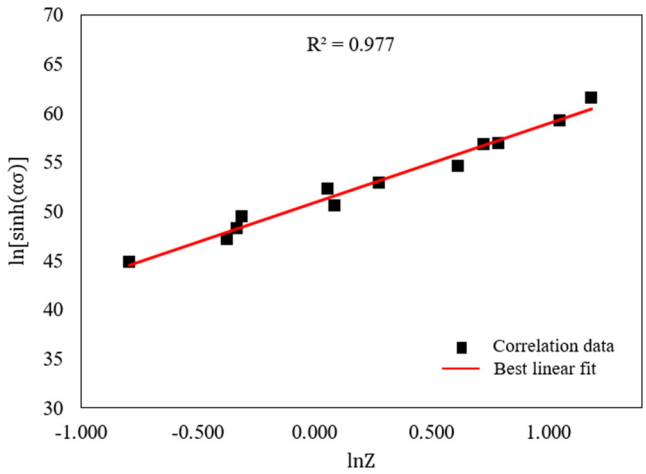

Fig. 6 The relationship between $\ln Z$ and $\ln[\sinh(\alpha\sigma)]$, used to calculate A

Finally, for every strain rate, Eq. (1) can be reformulated as follows:

$$Z = \dot{\varepsilon}\exp(Q/RT) = A\left[\sinh(\alpha\sigma)\right]^{n_2} \tag{15}$$

$$\ln Z = \ln A + n_2 \ln\left[\sinh(\alpha\sigma)\right] \tag{16}$$

Based on the experimental results for the relationship between $\ln Z$ and $\ln[\sinh(\alpha\sigma)]$ in Fig. 6, it is possible to create a linear plot with $\ln A$ as the y-axis intercept. Thus, the value of A, obtained by linear regression, is 1.2421×10^{22} s^{-1}.

3.3. Comparing the experimental true stress-strain curve with the predicted curve obtained using the Arrhenius model with the Zener-Hollomon parameter

The flow stress of the AISI 1045 medium carbon steel can be determined using the Arrhenius model with the Zener-Hollomon parameter. The constitutive equation for this steel can be expressed as:

$$\sigma = \frac{1}{\alpha}\ln\left\{\left(\frac{Z}{A}\right)^{1/n} + \left[\left(\frac{Z}{A}\right)^{1/n} + 1\right]^{1/n}\right\} \tag{17}$$

The experimentally measured and predicted flow stress-strain curves obtained under various conditions are compared in Fig. 7. According to the previous studies [5, 10, 22-23], the high accuracy of prediction is evaluated by the correlation coefficient (R^2) and AARE values, which are found to be 0.968 and 7.079%, respectively (Fig. 8).

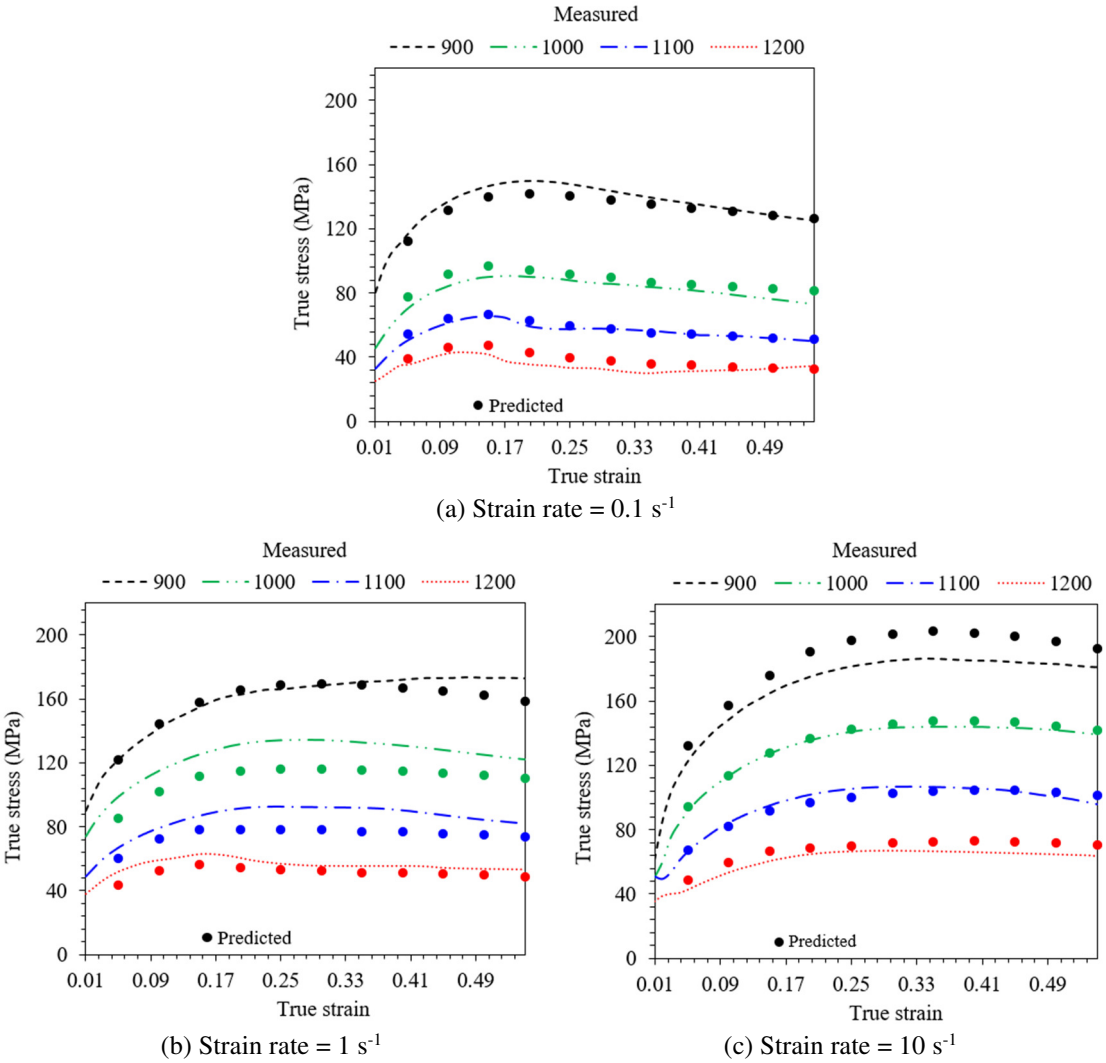

(a) Strain rate = 0.1 s^{-1}

(b) Strain rate = 1 s^{-1}

(c) Strain rate = 10 s^{-1}

Fig. 7 Comparison of flow curves using the Arrhenius model with Zener-Hollomon parameter

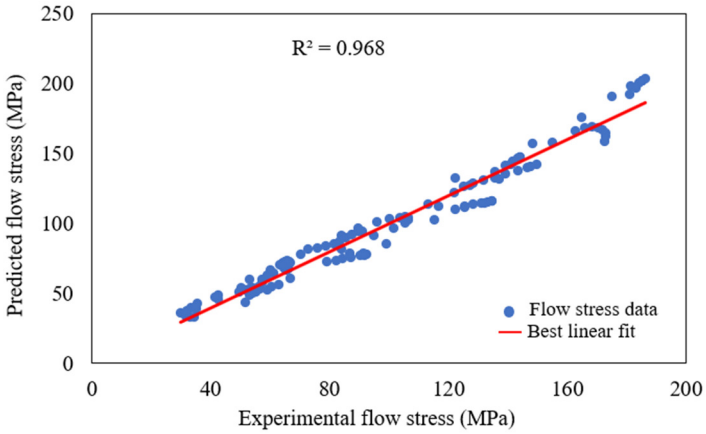

Fig. 8 Comparison of experimental results and Arrhenius model predictions with Zener-Hollomon parameter

3.4. *Modeling the material flow behavior by using the Cingara-McQueen equation and considering the work-hardening range*

The flow curve depicting the relationship between true stress and true strain, as obtained from material testing, can be used to construct a predictive model of the strain-hardening flow behavior by employing the Cingara-McQueen equation [21, 24-26].

$$\sigma = \sigma_p \left[\left(\frac{\varepsilon}{\varepsilon_p} \right) \exp\left(1 - \frac{\varepsilon}{\varepsilon_p} \right) \right]^C \tag{18}$$

"*C*" represents the material's constant value. The mathematical model for strain-hardening flow behavior is constructed, starting from the initial stress value, employing the Cingara-McQueen equation described in Eq. (18). Subsequently, the natural logarithm of this equation is applied to describe the behavior up to the point of peak stress.

$$\ln\left(\frac{\sigma}{\sigma_p} \right) = C \left[1 - \frac{\varepsilon}{\varepsilon_p} + \ln\left(\frac{\varepsilon}{\varepsilon_p} \right) \right] \tag{19}$$

Utilizing Eq. (19), a model for the flow behavior can be established up to the point of peak stress by plotting $\ln(\sigma/\sigma_p)$ and $1 - (\varepsilon/\varepsilon_p) + \ln(\varepsilon/\varepsilon_p)$, then, deducing the constant value *C* (Fig. 9). This modeling incorporates deformation conditions and is subsequently compared with experimental results and the average *C* value, as detailed in Table 3.

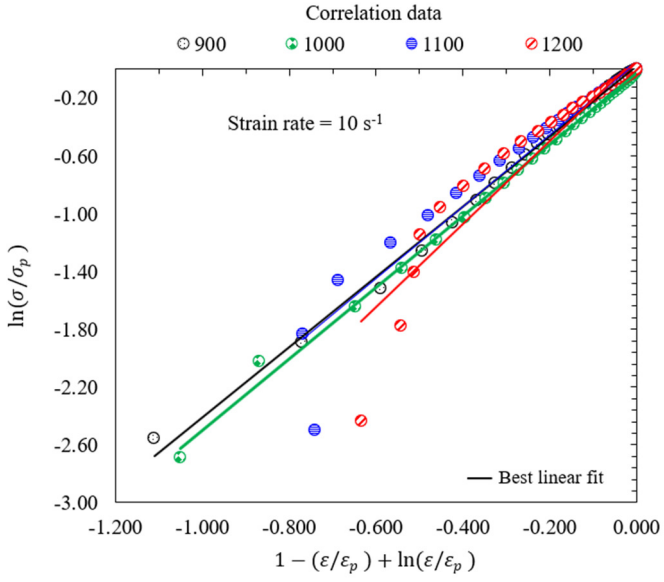

Fig. 9 The linear plot for calculating the constant *C* in the Cingara-McQueen equation

Table 3 The constant value "*C*" in the Cingara-McQueen equation

Temperature (°C)	Strain rate (s^{-1})	Peak stress (MPa)	Peak strain	Cingara-McQueen constant *C*
900	0.1	149.6796265	0.20	0.312091341
1000	0.1	90.38090324	0.18	0.375450371
1100	0.1	65.35096447	0.15	0.406464783
1200	0.1	43.00867550	0.11	0.360676540
900	1	173.4728917	0.48	0.238875480
1000	1	134.7181396	0.28	0.277197960
1100	1	92.54732514	0.24	0.312320588
1200	1	62.87665939	0.16	0.288906917
900	10	186.4152832	0.34	0.410286431
1000	10	144.0617676	0.39	0.403633354
1100	10	106.6663183	0.32	0.377293594
1200	10	66.63057200	0.30	0.314228333

The true stress-true strain curves obtained from the experimental results are compared with the corresponding predictions obtained from the Cingara-McQueen equation in Fig. 10. Moreover, the validity of the Cingara-McQueen equation as a reliable constitutive model is confirmed by the linear analysis of the AISI 1045 material behavior shown in Fig. 11, with R^2 and AARE values of 0.997 and 2.960%, respectively.

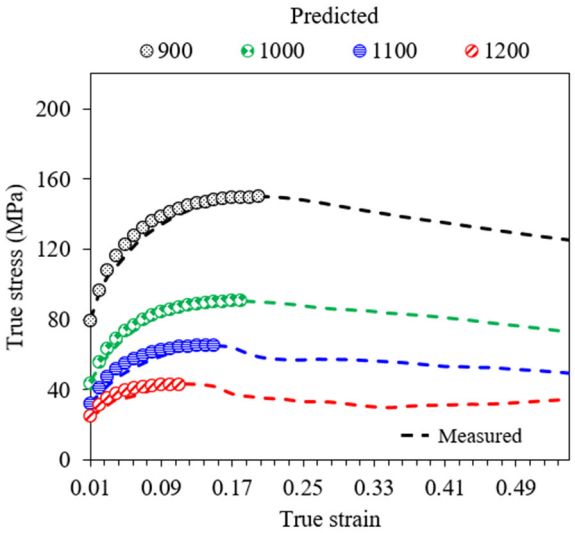

(a) Strain rate = 0.1 s^{-1}

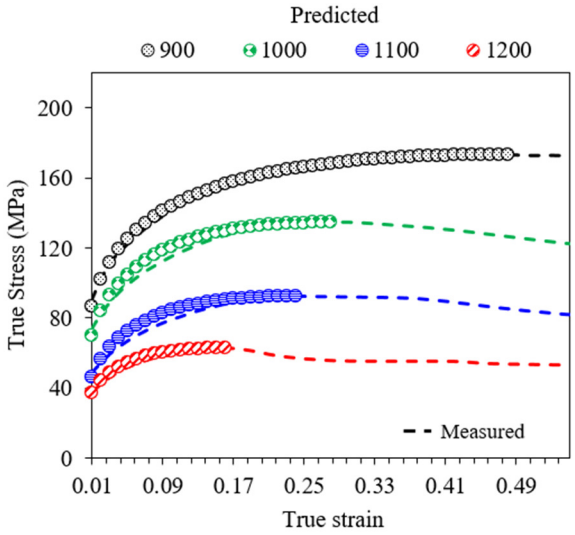

(b) Strain rate = 1 s^{-1}

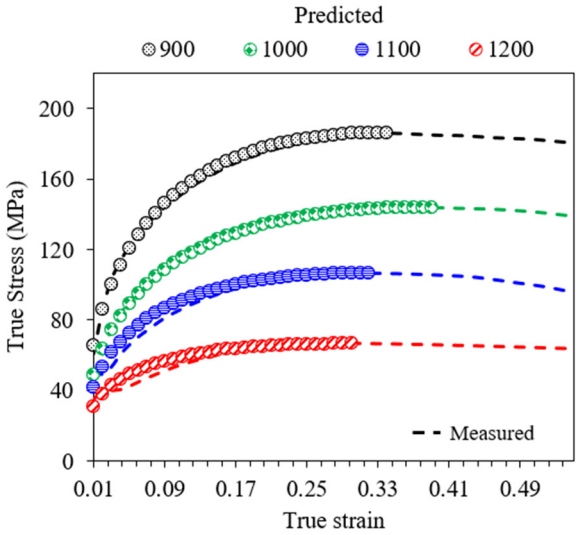

(c) Strain rate = 10 s^{-1}

Fig. 10 Comparison of flow curves using the Cingara-McQueen equation (continued)

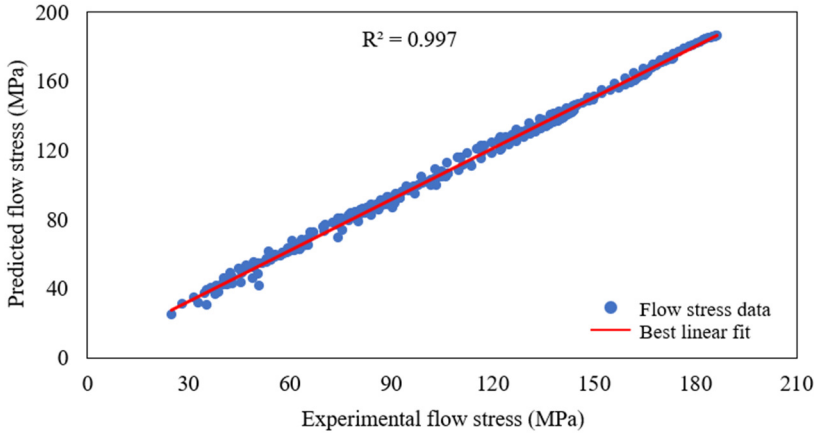

Fig. 11 The best linear fit of the experimental results to the Cingara-McQueen equation

4. Experimental Design

Numerous attempts have been made to predict metal flow behavior when studying various aspects of the forging process. In line with these efforts, Jantepa and Suranuntchai [27] used the FEM to optimize a hot forging die for producing a ball joint automotive part, aiming to enhance production efficiency, extend the machine life, and ensure defect-free workpieces. Key parameters were studied and optimized, including the die gap (4, 3, and 2 mm) and forming load (not exceeding 85% of machine capability). The FEM simulation revealed that a die gap of 3 mm is optimal in both the roughing and finishing processes, resulting in defect-free workpieces within specifications, along with forming loads below 85%.

After evaluating the AISI 1045 material properties under high-temperature conditions and using mathematical modeling to predict the material flow behavior using the Zener-Hollomon and Cingara-McQueen equations as detailed above, the data obtained herein were subjected to actual testing with workpieces designed using finite element software. This was done to validate the models by comparing their theoretical results with those of actual experiments. The workpiece prototypes, material testing data, and experimental design are briefly described in the following paragraphs.

(1) Workpiece prototypes for testing purposes

For testing, authentic ball joint prototypes that were engineered to endure the impact forces encountered in automobiles were used. The key features of these prototypes are outlined in Fig. 12(a), while the initial billet dimensions for fabricating the actual workpiece are shown in Fig. 12(b). It should be noted that the appropriate billet size was identified by a process of trial and error without dependence on any material testing data.

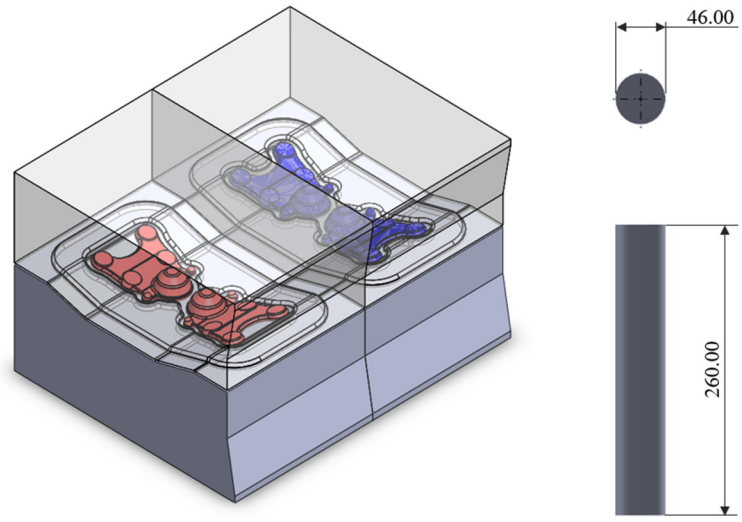

(a) Workpiece prototypes (b) Current billet size

Fig. 12 Workpiece prototypes for testing purposes

(2) Material testing data for modeling

The material testing data for the AISI 1045 were imported into the finite element modeling software. These data included the specific chemical composition, high-temperature flow behavior, and various flow rate values, along with other relevant information.

(3) Experimental design

The experimental design involves varying the initial size of the billet used in the manufacture of the workpiece to minimize production costs and address concerns related to die damage caused by workpiece deformation. As shown in Fig. 13, three initial billet lengths (230, 240, and 260 mm) were tested, with a constant diameter of 46.00 mm, and the forging temperature was maintained at 1200 ℃, serving as both the actual production temperature and the standard testing temperature for materials under high-temperature conditions. It should be noted that the maximum initial billet length (260 mm) was selected by trial and error without any reference to published material testing data.

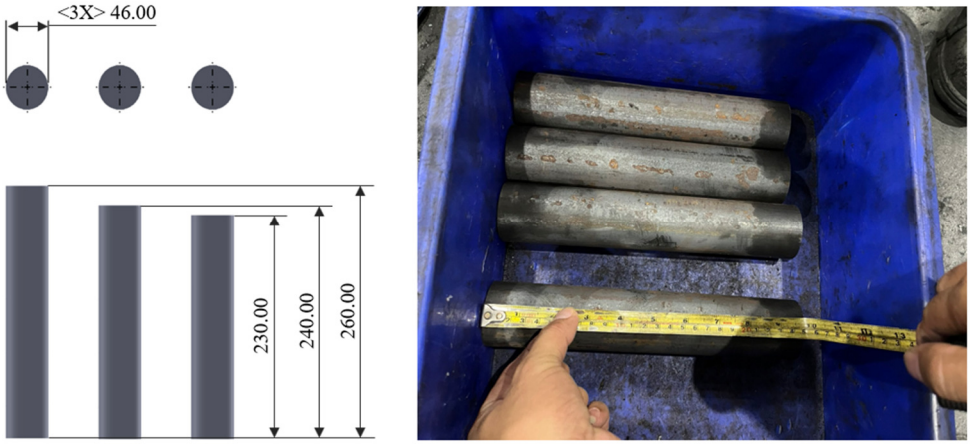

Fig. 13 The billet sizes used for the experiments

5. Experimental Result

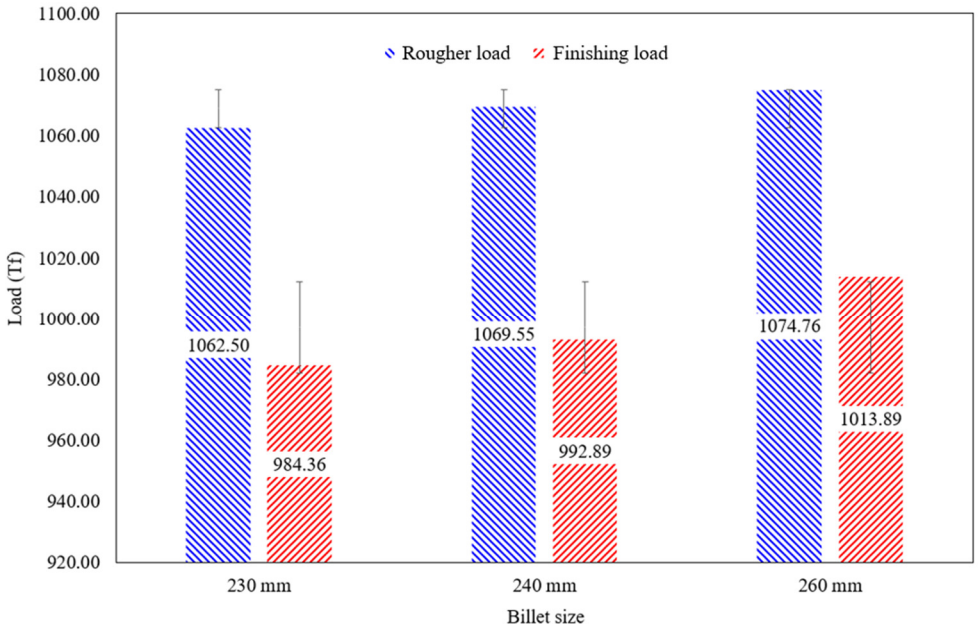

Fig. 14 Experimental load variation by billet size

For each of the three billet lengths (260, 240, and 230 mm), tests were conducted to collect data on the applied loads during the roughing and finishing processes on a 1350-ton mechanical press. The results are presented as a bar chart in Fig. 14. Here, the 260 mm billet size exhibits the highest forging load, with roughing and finishing loads of 1062.50 and 984.36

Tf, respectively. Conversely, the lowest load is observed for the 230 mm billet size, with roughing and finishing loads of 1074.76 and 1013.89 Tf. During the roughing process, the material undergoes significant deformation as it is shaped into the initial form, thus requiring higher forces. By contrast, the finishing process involves refining the already-shaped workpiece, which requires less material deformation and, hence, lower forces.

The FEM simulation was also performed for the three initial billet lengths, and the simulation results are compared with the experimental results in Table 4. Thus, in the roughing process, the maximum percentage error between simulation and experiment (i.e., 2.80%) is observed for the 260 mm billet size, while the minimum error (2.51%) is observed for the 230 mm billet size. Similarly, in the finishing process, the maximum error (3.29%) is observed for the 260 mm billet size, and the minimum error (2.25%) is observed for the 240 mm billet size. Overall, an average error of about 2.69% is observed across all billet sizes, and the processes fall within an acceptable range. These results underscore the consistency and reliability of the simulation model in predicting the applied loads during both the roughing and finishing processes, thereby enhancing the understanding of these processes.

Table 4 A comparison of the experimental and simulated loads

Billet size (mm)	Roughing load		%Error	Finishing load		%Error
	Actual test (Tf)	Simulation (Tf)		Actual test (Tf)	Simulation (Tf)	
230	1062.50	1035.78	2.51%	984.36	959.32	2.54%
240	1069.55	1040.12	2.75%	992.89	970.52	2.25%
260	1074.76	1044.70	2.80%	1013.89	980.55	3.29%

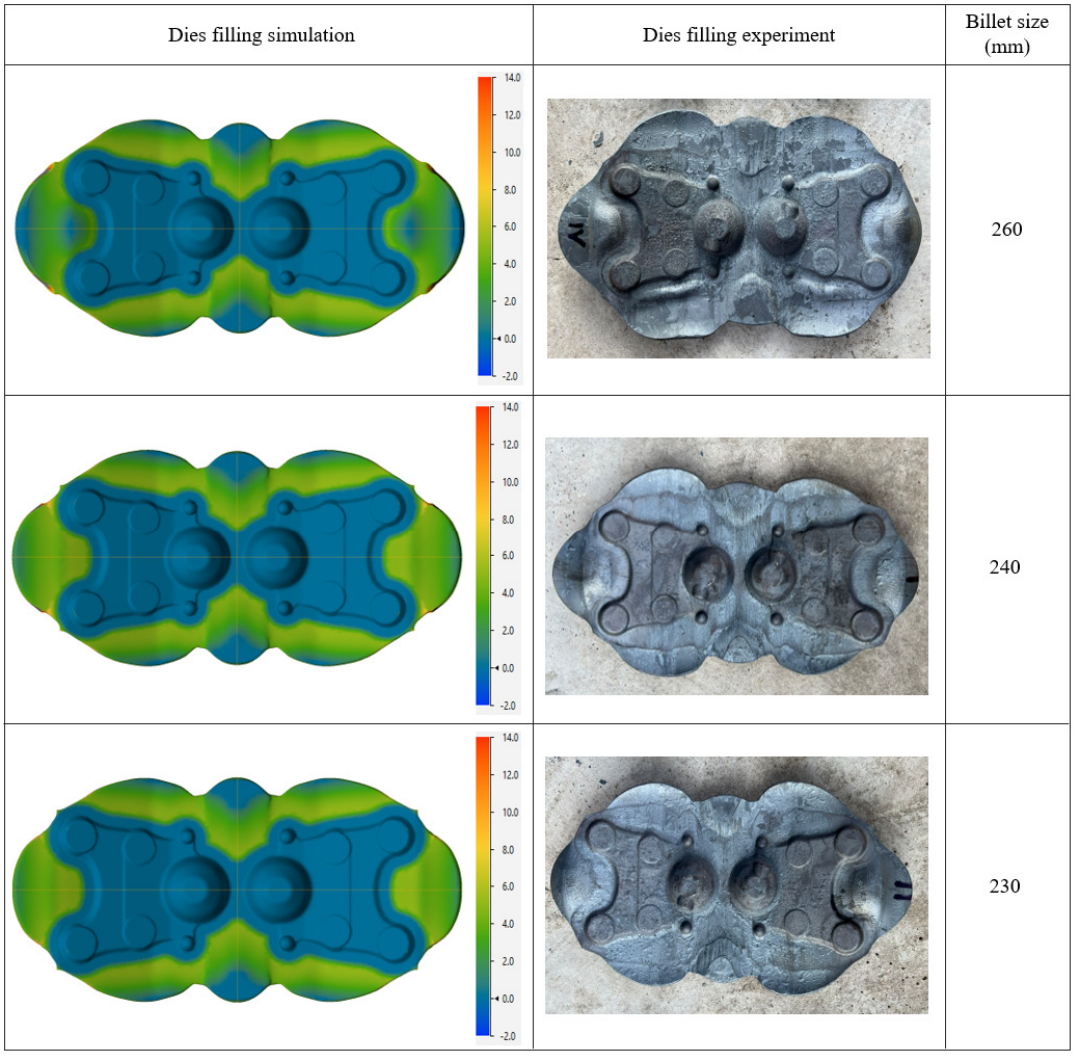

Fig. 15 The effect of billet size on die filling completeness in the simulation (left) and experiment (right)

To evaluate the loads during forming, it is essential to determine whether the billet size ensures complete die-filling and whether the die is affected by any abnormal flash characteristics. In this respect, the experimental results indicate that the studied billet sizes have no discernible effect on die filling. As shown in Fig. 15, each workpiece is fully constructed and has no obvious defects, thereby indicating complete contact with the die cavity. In addition, Fig. 15 compares the final forged part with the simulation results, where the distance between the tools and the outer surface of the workpiece is indicated by the color contours.

Here, it can be seen that the flash area is larger in the actual forming part than in the simulation. This might be due to temperature variations in the actual forging process, which can influence the material behavior and consequently affect the size of the flash produced during forming. In particular, the 260 mm billet size exhibits a relatively large flash area, thus leading to material wastage. In addition, the FEM results in Fig. 16 indicate the presence of bending at the flash area after the finishing process for the 260 mm billet, which results in collision with, and subsequent damage of, the die. By contrast, the 230 mm billet exhibits a smaller flash area and maintains a smoother surface without deformation during forming. As a result, this condition prevents die damage and reduces material wastage.

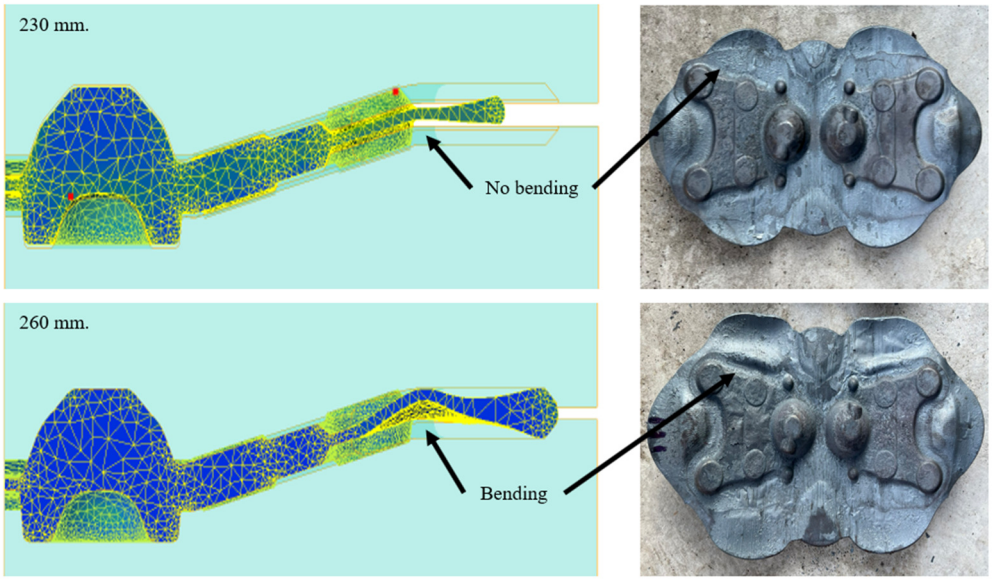

Fig. 16 FEM analysis of die filling with varied billet size and flash area evaluation

6. Conclusions

Herein, key findings on various aspects of the current industrial hot forging process are presented, including material properties, production capabilities, and suitable billet size optimization for cost reduction. The key findings are as follows:

(1) Material testing, chemical composition analysis, and high-temperature compressive testing demonstrate the effective utilization of material data in mathematical modeling and process simulation, mainly through FEM. The experimentally obtained flow curves align well with the predictive outcomes using both the Zener-Hollomon and Cingara-McQueen approaches. Notably, the study showcases the accuracy of predicting the flow stress of AISI 1045 steel by using the Arrhenius model with the Zener-Hollomon parameter, supported by an R^2 value of 0.968 and an AARE of 7.079%. Additionally, validation of the Cingara-McQueen equation against experimental results yields an R^2 of 0.997 and an AARE of 2.960%, thus confirming its reliability as a constitutive model for material behavior analysis.

(2) The experimental testing and FEM simulation results revealed that reducing the billet size from 260 mm to 230 mm leads to a consistent decrease in applied loads during both roughing and finishing processes. The 260 mm billet size showed the highest forging load, while the 230 mm billet size exhibited the lowest load. Even with variations in billet size, the FEM

analysis showed an average error of about 2.69%, thus affirming the reliability of the simulation predictions. The results suggest that the machinery load capacity remains unaffected by differences in billet size, thereby aiding in the validation of simulation data against experimental results.

(3) Each billet size achieves complete die filling. However, the larger flash area associated with the 260 mm billet size leads to bending and damage to the die.

In conclusion, the experimental data show that the billet size used in the ball joint forming process can be effectively reduced without compromising the quality of the resulting workpiece or the production process. This reduction lowers the production costs and enhances the competitiveness of this process in the industrial sector.

Acknowledgments

This research project is supported by the National Research Council of Thailand (NRCT): NRCT5-RRI63006-P08 for financial support. Also, sincere gratitude must be given to "S.B. - CERA Co., Ltd." for the material testing and the experiment part.

Conflicts of Interest

The authors declare no conflict of interest.

References

[1] T. Altan, G. Ngaile, and G. Shen, Cold and Hot Forging: Fundamentals and Applications, Materials Park, OH: ASM International, 2005.

[2] N. S. Al-Arifi, A. S. Zamani, and J. Khan, "Billet Optimization for Steering Knuckle Using Taguchi Methodology," International Journal of Computer Theory and Engineering, vol. 3, no. 4, pp. 552-556, August 2011.

[3] P. Soranansri, T. Rojhirunsakool, N. Nithipratheep, C. Ngaouwnthong, K. Boonpradit, C. Treevisootand, et al., "Hot Forging Process Design and Initial Billet Size Optimization for Manufacturing of the Talar Body Prosthesis by Finite Element Modeling," Applied Science and Engineering Progress, vol. 15, no. 1, article no. 3936, January-March 2022.

[4] N. Siripath, S. Suranuntchai, and S. Sucharitpwatskul, "Cylindrical Billet Size Optimization for Hot Closed-Die Forging of the Upper Ball Joint," Key Engineering Materials, vol. 946, pp. 9-14, May 2023.

[5] S. S. Satheesh Kumar, T. Raghu, P. P. Bhattacharjee, G. Appa Rao, and U. Borah, "Constitutive Modeling for Predicting Peak Stress Characteristics during Hot Deformation of Hot Isostatically Processed Nickel-Base Superalloy," Journal of Materials Science, vol. 50, no. 19, pp. 6444-6456, October 2015.

[6] S. A. Kareem, J. U. Anaele, E. O. Aikulola, O. F. Olanrewaju, B. O. Omiyale, M. O. Bodunrin, et al., "Hot Deformation Behaviour, Constitutive Model Description, and Processing Map Analysis of Superalloys: An Overview of Nascent Developments," Journal of Materials Research and Technology, vol. 26, pp. 8624-8669, September-October 2023.

[7] H. Zhu and H. Ou, "Constitutive Modelling of Hot Deformation Behaviour of Metallic Materials," Materials Science and Engineering: A, vol. 832, article no. 142473, January 2022.

[8] G. Ge, L. Zhang, J. Xin, J. Lin, M. Aindow, and L. Zhang, "Constitutive Modeling of High Temperature Flow Behavior in a Ti-45Al-8Nb-2Cr-2Mn-0.2Y Alloy," Scientific Reports, vol. 8, article no. 5453, 2018.

[9] N. Siripath, S. Suranuntchai, and S. Sucharitpwatskul, "Comparative Study on Material Models for BS 080M46 Medium Carbon Steel," Engineering & Applied Science Research, vol. 51, no. 1, pp. 22-33, January-February 2024.

[10] J. Zhang, H. Di, X. Wang, Y. Cao, J. Zhang, and T. Ma, "Constitutive Analysis of the Hot Deformation Behavior of Fe–23Mn–2Al–0.2C Twinning Induced Plasticity Steel in Consideration of Strain," Materials & Design, vol. 44, pp. 354-364, February 2013.

[11] Z. S. Motlagh, B. Tolaminejad, and A. Momeni, "Prediction of Hot Deformation Flow Curves of 1.4542 Stainless Steel," Metals and Materials International, vol. 27, no. 8, pp. 2512-2529, August 2021.

[12] N. Jantepa and S. Suranuntchai, "Investigation of Hot Deformation Behavior of SNCM8 Alloy Steel," World Journal of Mechanics, vol. 11, no. 03, pp. 17-33, March 2021.

[13] G. Wei, X. Peng, A. Hadadzadeh, Y. Mahmoodkhani, W. Xie, Y. Yang, et al., "Constitutive Modeling of Mg–9Li–3Al–2Sr–2Y at Elevated Temperatures," Mechanics of Materials, vol. 89, pp. 241-253, October 2015.

[14] A. Sanrutsadakorn, V. Uthaisangsuk, and S. Suranuntchai, "Determination of Initiation of Dynamic Recrystallization in AISI 4340 Steel," Advanced Materials Research, vol. 893, pp. 381-386, February 2014.

[15] I. Schindler, P. Opěla, P. Kawulok, J. Sojka, K. Konečná, S. Rusz, et al., "Hot Deformation Behaviour of Mn–Cr–Mo Low-Alloy Steel in Various Phase Regions," Metals, vol. 10, no. 9, article no. 1255, September 2020.

[16] R. B. Prajapati, D. B. Patel, and T. M. Patel, "A Review on Experimental Investigation of GMAW for AISI 1045 by Using Taguchi Method," International Journal for Scientific Research & Development, vol. 1, no. 8, pp. 1679-1682, 2013.

[17] P. Jedrasiak, H. Shercliff, S. Mishra, C. S. Daniel, and J. Q. da Fonseca, "Finite Element Modeling of Hot Compression Testing of Titanium Alloys," Journal of Materials Engineering and Performance, vol. 31, no. 9, pp. 7160-7175, September 2022.

[18] A. Sanrutsadakorn, V. Uthaisangsuk, S. Suranuntchai, and B. Thossatheppitak, "Constitutive Modeling of Flow Behaviour of AISI 4340 Steel Under Hot Working Conditions," Applied Mechanics and Materials, vol. 249-250, pp. 863-869, December 2012.

[19] N. Siripath, S. Suranuntchai, and S. Sucharitpwatskul, "Finite Element Modeling of Upper Ball Joint in a Two-Step Hot Forging Process," Key Engineering Materials, vol. 934, pp. 95-102, November 2022.

[20] A. Hajari, M. Morakabati, S. M. Abbasi, and H. Badri, "Constitutive Modeling for High-Temperature Flow Behavior of Ti-6242S Alloy," Materials Science and Engineering: A, vol. 681, pp. 103-113, January 2017.

[21] M. S. Ghazani and B. Eghbali, "Modeling the Flow Behavior of AISI 321 Austenitic Stainless Steel Using a Simple Combined Phenomenological Method," Mechanics of Materials, vol. 137, article no. 103108, October 2019.

[22] N. Haghdadi, A. Zarei-Hanzaki, and H. R. Abedi, "The Flow Behavior Modeling of Cast A356 Aluminum Alloy at Elevated Temperatures considering the Effect of Strain," Materials Science and Engineering: A, vol. 535, pp. 252-257, February 2012.

[23] L. Wang, F. Liu, Q. Zuo, and C. F. Chen, "Prediction of Flow Stress for N08028 Alloy under Hot Working Conditions," Materials & Design, vol. 47, pp. 737-745, May 2013.

[24] J. Porntadawit, V. Uthaisangsuk, and P. Choungthong, "Modeling of Flow Behavior of Ti–6Al–4V Alloy at Elevated Temperatures," Materials Science and Engineering: A, vol. 599, pp. 212-222, April 2014.

[25] K. B. Kumar, K. K. Saxena, S. R. Dey, V. Pancholi, and A. Bhattacharjee, "Peak Stress Studies of Hot Compressed TiHy 600 Alloy," Materials Today: Proceedings, vol. 4, no. 8, pp. 7365-7374, 2017.

[26] G. L. Wu, Y. J. Zhang, and S. W. Wu, "Characterization of Hot Deformation Behaviour of Nb-Ti Microalloyed High-Strength Steel," Journal of the Southern African Institute of Mining and Metallurgy, vol. 119, no. 5, pp. 503-508, May 2019.

[27] N. Jantepa and S. Suranuntchai, "Finite Element Simulation of Ball Joint under Hot Forging Process," Journal of Physics: Conference Series, vol. 1510, article no. 012013, 2020.